Observed equatorial Rossby waves and ENSO-related warm water volume changes in the equatorial Pacific Ocean

Christelle Bosc[1] and Thierry Delcroix[1]

[1]   Modifications of the volume of warm water above the thermocline in the equatorial Pacific are thought to be critical for ENSO (El Niño Southern Oscillation) preconditioning, development and prediction. In this paper, changes in this Warm Water Volume (WWV) are first reviewed from the literature, and then analyzed within 5°N–5°S in using 1992–2006 altimeter-derived sea level anomalies (SLA) and in situ observations. We conclude that the 1992–2006 WWV changes in the equatorial band are a residual from the opposite effects of zonally integrated meridional Ekman and geostrophic transports of warm water, the latter being estimated from SLA and validated against in situ observations. For the first time with observations, we evidence first baroclinic first meridional mode equatorial Rossby waves to be responsible for the anomalous meridional geostrophic transports of warm water, in changing the basin-scale zonal pressure gradient. These transports appear in phase opposition and proportional to the anomalous Sea Surface Temperature (SST) in the region NIÑO3.4 (170°W–120°W, 5°N–5°S). The links between our observational results and the recharge/discharge oscillator theory, the differences in WWV between ENSO events, and the hint for possible recent changes in the relation between WWV and NIÑO3.4 SST are discussed.

1.   Introduction

[2]   The El Niño Southern Oscillation (ENSO) event represents the most energetic year-to-year climate variation in the tropical Pacific, with many adverse or beneficial environmental and socio-economic impacts at global scale [*Philander*, 1990; *Glantz*, 1996; *Goddard and Dilley*, 2005; *McPhaden et al.*, 2006a]. Owing to tremendous progress in monitoring, understanding, modeling and forecasting ENSO in recent years, the ENSO basic physics is now *relatively* well understood. In particular, four major theories were proposed to account for its quasi-cyclic nature with periods of 3–7 years: the delayed action oscillator [*Suarez and Schopf*, 1988], the western Pacific oscillator [*Weisberg and Wang*, 1997], the advective-reflective oscillator [*Picaut et al.*, 1997], and the recharge–discharge (RD) oscillator [*Jin*, 1997]. A proposed unified theory and a review of theses four theories are given by *Wang* [2001] and *Wang and Picaut* [2004].

[3]   For El Niño events to develop, once started, these four theories all involve the same positive feedback [*Bjerknes*, 1969] in which westerly wind anomalies in the western equatorial Pacific and warm Sea Surface Temperature (SST) anomalies in the eastern equatorial Pacific reinforce each other, whatever the atmospheric or oceanic anomalies first appear. As a negative feedback, the first three theories only explicitly entail equatorial waves and their reflections at the western and/or eastern boundaries for the system to oscillate. Regarding the fourth theory (the RD oscillator), *Jin* [1997] noted that "the detail wave propagation process is not emphasized" even though equatorial waves are important in the adjustment of the equatorial ocean. Interestingly, the RD oscillator is also the only one theory to stress the need for an accumulation and depletion of mass in the equatorial band (in agreement with observations, see below), and so for a latitudinal mass exchange between the equatorial and off-equatorial regions for ENSO to be a cycle. These features of the RD oscillator are sketched in the schematic diagrams drawn by *Jin* [1997], *Meinen and McPhaden* [2001], and *Clarke et al.* [2007].

[4]   Studies that contributed to bring about and improve aspects of the RD oscillator have so far considered different variables: sea level, upper layer heat content, upper layer dynamic height anomalies, thermocline depth, and the related Upper Layer Volume (ULV) and/or Warm Water Volume (WWV). *Rébert et al.* [1985] showed from the analysis of in situ observations, at few locations, that these variables generally agree well in the tropical Pacific. In particular, the agreement between sea level and thermocline depth (and so WWV) was found much better in the equatorial band because the ocean there does behave like a 1.5 layer ocean system given the well-marked thermocline. In the following paragraph, the discussion

[1]Laboratoire d'Etudes en Géophysique et Océanographie Spatiales (LEGOS), CNES/CNRS/IRD/UPS, Toulouse, France.
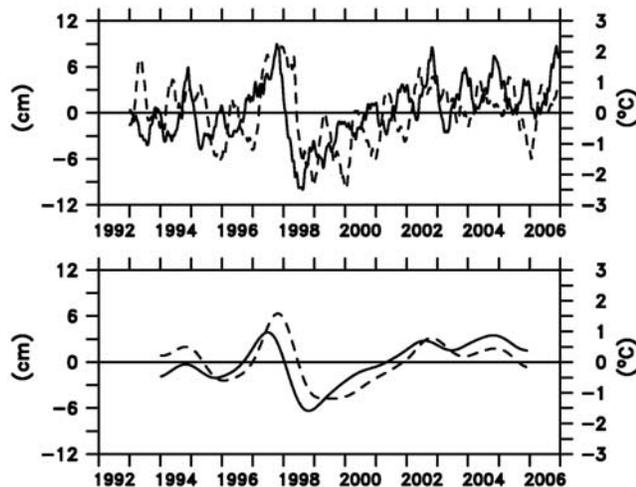
Figure 1. Time series of sea level anomalies averaged within 5°S–5°N, 120°E–80°W (full lines, left vertical axes, units are in centimeters) and NIÑO3.4 SST anomalies averaged within 5°S–5°N, 170°W–120°W (dashed lines, right vertical axes, units are in Celsius). The anomalies are relative to the 1993–2006 time period. The top panel shows weekly values, and the bottom panel shows the interannual variations estimated by filtering the weekly values with a 105-week Hanning filter.

of some background findings regarding aspects of the RD oscillator should thus consider all these variables as being interchangeable.

[5] The RD oscillator roots on the early results of *Wyrtki* [1985]. This author showed that the so-called ULV, as estimated from 1975–1983 scattered island-based sea level measurements, builds up within 15°S–15°N prior to the moderate 1976–1977 and very strong 1982–1983 El Niño events, and then drops off during the mature phases with a move of the above normal ULV to higher latitudes. On the basis of the 1985–1989 more uniformly distributed GEO-SAT sea level measurements, *Miller and Cheney* [1990] found that the ULV did decrease following the 1987–1988 El Niño, though only within about 8°N–8°S latitude of the equator and with a corresponding rise in the northern tropical zone only. In using a simple coupled model, *Zebiak and Cane* [1987] and *Zebiak* [1989] established that above normal heat content in the equatorial band is a necessary, though not sufficient, condition for El Niño event to occur. *Zebiak* [1989] showed, in particular, that at the ENSO timescale, changes in heat content within 15°S–5°S and 5°N–5°S are almost in phase, and both latitudinal bands are out-of-phase with the one within 5°N–15°N. Latter on, *Delcroix* [1998] and *Meinen and McPhaden* [2000] analyzed 15–20 yearlong changes in 0/450 dbar dynamic height anomalies and WWV (i.e., the volume of "warm" water above the thermocline chosen as the depth of the 20°C isotherm), respectively. They found two primary modes of ENSO variability: a well-known east-west tilting mode in the equatorial band, and a RD mode which redistributes WWV between about 15°S–5°N and 5°N–20°N. *Alory and Delcroix* [2002] reached similar conclusions with the 1992–1999 Topex/Poseidon (TP) sea level measurements, and a 1964–1999 validated linear model

simulation of sea level. Interestingly, these last studies concluded that the RD mode leads the tilting mode by about half a year. Moreover, they confirmed that the RD mode is by far not symmetrical about the equator, and specifically that the WWV is chiefly redistributed between the two 20°S–5°N and 5°N–20°N latitudinal bands at the ENSO timescale, with the largest changes occurring within 5°N–5°S. *Meinen and McPhaden* [2001] then evidenced that the 1993–1999 observed WWV changes in an equatorial box (156°E–95°W, 8°N–8°S) are concurrent with ENSO, and mostly result from Ekman and geostrophic transports across the lateral box boundaries, with the meridional transports dominating. A consistent result was obtained by *Meinen* [2005] for the 1993–2003 period, in using a slightly different equatorial box (bounded at 5°N–5°S instead of 8°N–8°S) and a combination of hydrography, altimeter-derived sea level and Sverdrup transport calculations.

[6] While ENSO is the most predictable year-to-year climate change on Earth, current ENSO forecasts still need to be improved either from statistical or dynamical models [e.g., *Kirtman et al.*, 2001]. The potential for predictions relies, at least, on the knowledge of: westerly wind anomalies and/or Madden Julian Oscillation (MJO) activities in the western equatorial Pacific [*Slingo et al.*, 1999; *McPhaden et al.*, 2006b], zonal displacements of the eastern edge of the western Pacific warm pool [*Clarke and Van Gorder*, 2001], SST anomalies in the south-eastern tropical Indian ocean [*Terray and Dominiak*, 2005], and changes in the WWV of the equatorial Pacific [*Zebiak and Cane*, 1987; *McPhaden et al.*, 2006b]. That last predictor highlights the importance of the equatorial band in the RD oscillator theory. To illustrate its value, Figure 1 compares the 1992–2006 time series of sea level (a proxy for WWV, see below) averaged in the whole equatorial band and SST anomalies averaged in the NIÑO3.4 box (see the caption for details). The best correlation between the two interannual time series is R = 0.87, obtained when the sea level leads the SST changes by 21 weeks (about 5 months). (Unless mentioned otherwise, all correlations in the paper are statistically significant at the 95% confidence level after taking into account the autocorrelations of time series [see *Emery and Thomson*, 1998]). Noteworthy, the largest time lag occurred during the 1997–98 El Niño event, and the agreement applies in phase but not in amplitude as sea level and SST anomalies are not strictly proportional (as discussed below).

[7] As noted above, some interesting aspects of the RD oscillator conceptual model are: the unnecessary need to track equatorial wave propagations and their reflections, the requirement for a latitudinal mass exchange for ENSO to oscillate, an intrinsic potential for the prediction of the El Niño phase, and (not mentioned before) its likely relevance at decadal timescale [*Hasegawa and Hanawa*, 2003; *Cibot et al.*, 2005]. These features all concern the equatorial band. Hence as a first step, the aim of the present study is to focus on mechanisms responsible for WWV changes in the equatorial region only. The use of satellite-derived sea level and wind products covering the 1992 to 2006 years will enable us to quantify WWV changes, to assess the relative contribution of Ekman and geostrophic transports of warm water in these changes, and most of all, for the first time to our knowledge, to evaluate the role of *observed* equatorial

waves in the geostrophic transports involved in the RD of the equatorial band.

[8] The paper is organized as follows. Section 2 describes the data and data processing. Section 3 discusses the way we estimate Ekman transports, WWV, geostrophic currents *and* transports from sea level only, as well as the contribution of equatorial waves to these transports. Section 4 focuses on the key role of equatorial Rossby waves on WWV changes, compares WWV time series and spatial patterns for different El Niño episodes, and discusses the underlying mechanisms. A conclusion and discussion are then tackled in the last section.

2. Data and Data Processing

[9] Seven primary data sets are used in this study. The first data set is the Sea Level Anomaly (SLA) product generated by the AVISO altimetry program [*Ducet et al.*, 2000]. The SLA product is available onto $1/3°$ longitude by $1/3°$ latitude by one week grid mesh, and it includes the TOPEX/Poseidon and ERS1 or ERS2 data from October 1992, to August 2002, the Jason and ERS2 data from August 2002 to June 2003, and the Jason and ENVISAT data since June 2003. The SLA was computed relative to the 1993–2006 period. The second data set is the SST product available onto $1°$ longitude by $1°$ latitude by one week, from 1982 to the present time [*Reynolds et al.*, 2002]. The third data set is the $1/4°$ longitude by $1/4°$ latitude by one week wind stress data derived from the ERS and Quikscat satellites [*Bentamy et al.*, 1999], over the August 1991 to January 2001 and July 1999 to March 2007 period, respectively. The fourth data set is the monthly temperature measurements originating from the TAO-TRITON moorings within 8°N–8°S, as well as the monthly current measurements at the equator and 147°E, 156°E, 165°E, 140°W and 110°W [*McPhaden*, 1995]. Only the near-surface Acoustic Doppler Current Profiler (ADCP) measurements are considered here for the currents. The fifth data set is the 0.5° latitude by 5 m gridded current measurements obtained from a collection of 42 cruises carried out along the 165°E longitude during 1984–1992 [*Delcroix and Eldin*, 1995; *Delcroix and Picaut*, 1998]. The sixth data set is the 5° longitude by 1° latitude by 2 months gridded 20°C isotherm depth (Z_{20}), derived from XBT, TAO-TRITON and CTD measurements over the 1979–1992 period [*Durand and Delcroix*, 2000]. The last data set is the monthly values of the 1980–2007 WWV averaged within 120°E–80°W, 5°N–5°S, computed as by *Meinen and McPhaden* [2001] and made available on the Web (http://www.pmel.noaa.gov/tao/elnino/wwv/).

[10] The original SLA, SST and wind stress fields were reprocessed onto the same 1° longitude by 0.5° latitude by one week gridded fields in using subsampling technique or simple linear interpolations. The ERS wind product was further adjusted so that the mean ERS wind stress components equal the mean Quikscat components over the overlapping July 1999 to January 2001 period. The SLA, SST and wind stress gridded fields were finally smoothed with 11° longitude, 3.5° latitude and 5-week Hanning filters to reduce small-scale noise and/or possibly realistic physical high-frequency signals not considered here. Interannual variations discussed in Figure 1 and below were estimated

by filtering the weekly values with a 105-week (about 2 years) Hanning filter.

3. Methods

[11] This section details the way we estimate Ekman transports, (and validate) warm water volume, geostrophic surface currents and geostrophic transports from SLA, and the contribution of equatorial Rossby waves to the geostrophic transports.

3.1. Ekman Transports

[12] The zonal (U_e) and meridonal (V_e) Ekman transports are computed from the meridional (τ^y) and zonal (τ^x) wind stress, so that $U_e = \tau^y/\rho.f$ and $V_e = -\tau^x/\rho.f$, where ρ is the upper ocean density (taken as 1023 kg m^{-3}) and f is the Coriolis parameter [*Pond and Pickard*, 1983]. As discussed by *Meinen and McPhaden* [2001] and *Meinen* [2005], choosing other available wind products than the one used here does not significantly change the results as long as we are interested in the low frequency changes of the Ekman transports.

3.2. Warm Water Volume

[13] Following *Meinen and McPhaden* [2000], we define the WWV as the volume of warm water located above the thermocline (h). As noted in the Introduction, in the tropical Pacific, changes in the thermocline depth (h′) can be estimated from changes in sea level (η) with h′ = $-(\rho/\Delta\rho)\eta$. The WWV tendency for a given spatial domain delimited by eastern (E), western (W), northern (N), and southern (S) limits can then be estimated from sea level as:

$$\partial WWV / \partial t = (\rho/\Delta\rho)\partial/\partial t \left(\int_E^W \int_S^N \eta dx dy \right) \quad (1)$$

For three sites in the equatorial band, Santa Cruz, Christmas, and Kapingamarangi Islands, *Rébert et al.* [1985] showed that the values of $\rho/\Delta\rho$ range within 160 and 200. *Holland and Mitchum* [2003] used a value of $\rho/\Delta\rho = 200$ in updating to 1975–2002 the ULV time series originally derived by *Wyrtki* [1985]. An estimation of a mean $\rho/\Delta\rho$ value was established here for the 120°E–80°W, 5°N–5°S domain by comparing the 1992–2006 WWV computed from in situ thermocline depths (Z_{20}), as by *Meinen and McPhaden* [2001], versus the WWV computed from the areal integral of sea level as in equation (1). The best fit between the two time series was obtained with $\rho/\Delta\rho = 180$. Physically, it means that an increase of 10 cm in sea level corresponds to a deepening of 18 m in thermocline depth. With such a mean value for $\rho/\Delta\rho$, Figure 2 clearly evidences that altimeter-derived sea level is an excellent surrogate variable for WWV in the equatorial band (R = 0.86), in agreement with the results of *Meinen* [2005]. The small differences between the two curves reflect the contribution of salinity changes in sea level (not accounted for with in situ thermocline depth), the different sampling characteristics and errors of altimeter and in situ measurements, as well as the approximation of the true ocean as behaving like a 1.5 layer ocean model with a $\rho/\Delta\rho$ constant in time and space.
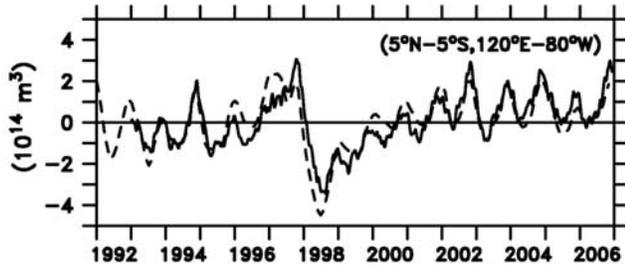
Figure 2. Time series of warm water volume anomalies averaged within 120°E–80°W, 5°N–5°S, as estimated from sea level (solid line) and in situ measurements (dashed line). The anomalies are relative to the 1993–2006 time period. Units are in 10^{14} m³.

3.3. Geostrophic Currents and Transports

[14] The zonal (U_g) and meridional (V_g) geostrophic transports of warm water across a meridional (y_0) or zonal (x_0) boundary are defined as:

$$Ug = \int_S^N \int_{z=0}^h u_g(x_0, y, z)dzdy \qquad (2a)$$

$$Vg = \int_E^W \int_{z=0}^h v_g(x, y_0, z)dzdx \qquad (2b)$$

[15] To estimate these transports from altimeter-derived sea level (η), we first computed the zonal (u_g) and meridional (v_g) geostrophic currents at the surface ($z = 0$) as:

$$f\, u_g = -g\, \partial\eta/\partial y, \text{ for } y \neq 0 \qquad (3a)$$

$$\beta\, u_g = -g\, \partial^2\eta/\partial y^2, \text{ for } y = 0 \qquad (3b)$$

$$f\, v_g = g\, \partial\eta/\partial x \qquad (3c)$$

where g is the acceleration due to gravity (9.81 m² s⁻²), and β the meridional derivative of the Coriolis parameter at the equator (2.28 10^{-11} rad s⁻¹ m⁻¹). Following *Picaut and Tournier* [1991], a correction factor C(y) was first added to the sea level field (η) to ensure continuity between u_g calculated from the first and second derivative calculations. That factor is expressed as:

$$C(y) = -(\partial\eta/\partial y)_{y=0} y e^{\left(-y^2/L^2\right)} \qquad (4)$$

Given the equations (3) and (4), u_g and v_g were calculated from the gridded sea level (η) using centered finite difference schemes, with a trapping scale L of 2° latitude. This method has proven quite efficient to estimate zonal surface current right at the equator [*Delcroix et al.*, 1994, 2000], despite the high sensitivity of u_g to small sea level error at this location. As a matter of fact, Figure 3 shows a

comparison between the longest time series of estimated and observed surface current at 0°–165°E during 1992–2006 (values at 35 m were used for the in situ measurements for completeness). The correlation coefficient and ratio of standard deviation are 0.81 and 0.85, respectively. Some statistics of comparisons for other mooring sites are given by *Delcroix et al.* [2000, Table 1] for the 1992–1998 period. We are thus now quite confident in our geostrophic surface currents derived from altimeter data.

[16] In order to evaluate the geostrophic transport in equation (2), it remains to estimate the integration depth (h), and the geostrophic velocities at any depth, knowing the surface geostrophic currents only. Several tests were made for determining the integration depth: constant values ranging from 50 to 150 m, spatially varying values based on $\bar{Z}_{20}(x, y)$ the 1979–1992 mean thermocline depth [*Durand and Delcroix*, 2000], and time-space varying values estimated from the mean thermocline depth $\bar{Z}_{20}(x, y)$ and the sea level (η) so that:

$$h(x, y, t) = \bar{Z}_{20}(x, y) + \frac{\rho}{\Delta\rho}\eta(x, y, t) \qquad (5)$$

[17] We also tried several hypotheses for the vertical profile of the geostrophic velocity: a constant velocity from the surface down to the thermocline (h), a linearly decreasing velocity from u_g at the surface to $u_g = 0$ at the thermocline depth (h), and a statistically derived velocity profile based on the linear regression between surface velocities and velocities at depth measured during western Pacific cruises [*Delcroix and Eldin*, 1995; *Delcroix and Picaut*, 1998]. The different possibilities for the integration depths and velocity profiles were combined, and the best choice was determined by comparing our geostrophic transport estimates with the ones obtained from in situ measurements across the boundaries of the 8°N–8°S, 156°E–95°W box [*Meinen and McPhaden*, 2001]. The best comparison was obtained in using an integration depth given in equation (5), a linear velocity vertical profile for the meridional transports, and a statistically derived vertical profile for the zonal transports. The comparisons are shown in Figure 4 for the meridional transports across the 8°N and 8°S latitudes. The correlation coefficients between the geostrophic transports derived from sea level only and the ones derived from in situ measurements are R = 0.94, 0.94, and
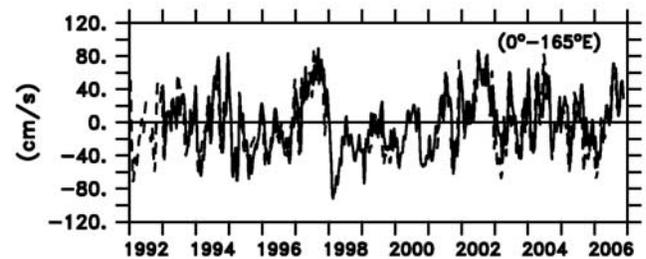
Figure 3. Comparison between altimeter-derived (solid line) and near-surface TAO/TRITON-derived zonal current anomalies (dashed line) at Eq.–165°E. The anomalies are relative to the overlapping time period of the years 1993–2006. Positive values denote eastward currents. Units are in cm/s.
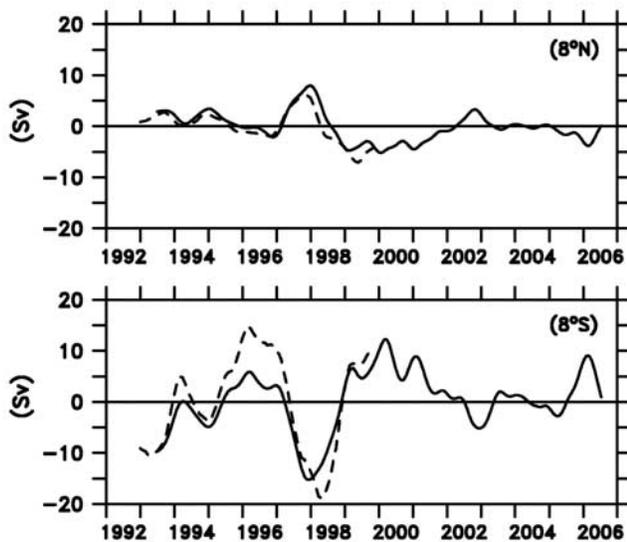
Figure 4. Time series of anomalous geostrophic transport of warm water across (top) 8°N and (bottom) 8°S, integrated from 156°E to 95°W. The full lines represent our estimated transport derived from sea level only and the best configuration of integration depth and vertical velocity profiles (see section 3). The dashed lines, running from 1993 to 1999, represent the transports calculated from in situ measurements only [see *Meinen and McPhaden*, 2000]. Note that a 20-week Hanning filter was applied on each estimated time series, to resemble the data processing performed by these last two authors. The anomalies are relative to the 1993–1999 common time period. Positive values denote northward transports. Units are in Sverdrups.

0.82, and the ratios of standard deviation are 1.0, 0.68, and 0.59, across 8°N, 8°S, and 156°E, respectively. The total geostrophic transports also compare quite well, with R = 0.91, and a ratio of 0.69. We are thus now rather confident in our geostrophic transports derived from altimeter data.

[18] The respective contribution of first baroclinic (c = 2.8 m s^{-1}) Kelvin and gravest Rossby modes to the surface current anomalies were obtained from sea level anomalies, following the method of *Delcroix et al.* [1994, 2000]. The contribution of the Kelvin and Rossby modes to the geostrophic *transports* was then estimated in using the integration depth in equation (5) and a first baroclinic mode mean vertical velocity profile. Details are given in the Appendix. Noteworthy, the first meridional mode (m = 1) Rossby wave results in meridional current anomalies which are maximum within 3–5° latitude and of opposite sign in the northern and southern hemispheres (Figure A1). As a remarkable consequence, downwelling (upwelling) Rossby waves will generate meridional geostrophic divergence (convergence) that will act to drain (fill up) the equatorial band. We will make use of this key feature in the following section.

## 4. Warm Water Volume, Meridional Transports and Equatorial Waves

4.1. Warm Water Volume and Meridional Transports

[19] Time series of the WWV changes derived from sea level was shown in Figure 2 for the 5°N–5°S, 120°E–80°W

domain. The time series is reproduced in Figure 5 and compared to the time-integrated net (geostrophic + Ekman) meridional transports of warm water across 5°N and 5°S, integrated from the western (120°E) to the eastern (80°W) Pacific boundaries. Figure 5 shows that the two estimates of WWV changes agree quite well. For the unfiltered data, the correlation coefficient and ratio of standard deviation ($\sigma_{vg+ve}/\sigma_{wwv}$) between the two time series are R = 0.79 and 1.6, respectively (0.82 and 1.3 at the interannual timescale). The small differences between the net meridional transports and WWV represent an estimate of the combined errors in: estimating WWV and meridional geostrophic transports from sea level only (see section 3), computing meridional Ekman transports from an inevitably imperfect wind field, and neglecting possible changes in cross-isothermal transports (see the discussion by *Meinen and McPhaden* [2001]). Regarding that last source of errors, there is no obvious link in Figure 5 between the magnitude of the differences between the two curves and the occurrence of ENSO events, suggesting that downward (upward) transports may not be enhanced during El Niño (La Niña) events at basin scale. Despite these small differences, the good accord in Figure 5 clearly shows that WWV changes result for a large part from the net convergence and divergence of meridional transports in the equatorial band during 1992–2006. Our results are consistent with the ones obtained from in situ measurements for shorter time periods and different spatial boxes (1992–1999 and 8°N–8°S, 156°E–95°W by *Meinen and McPhaden* [2001]; 1992–2003 and 5°N–5°S, 156°E–95°W by *Meinen* [2005]), as well as with Sverdrup (i.e., geostrophic + Ekman) transports determined in using wind observations only [*Meinen*, 2005].
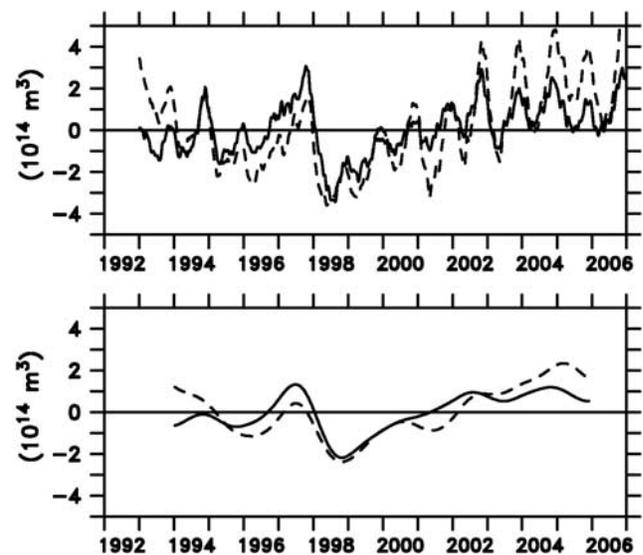
Figure 5. Time series of warm water volume anomalies, as estimated from (full lines) the sea level anomalies averaged within 120°E–80°W, 5°N–5°S, and (dashed lines) the net (geostrophic + Ekman) meridional transport anomalies entering the 5°N–5°S equatorial box. The top panel shows weekly values, and the bottom panel shows the interannual variations estimated by filtering the weekly values with a 105-week Hanning filter. The anomalies are relative to the 1993–2006 time period. Units are in 10^{14} m^3.
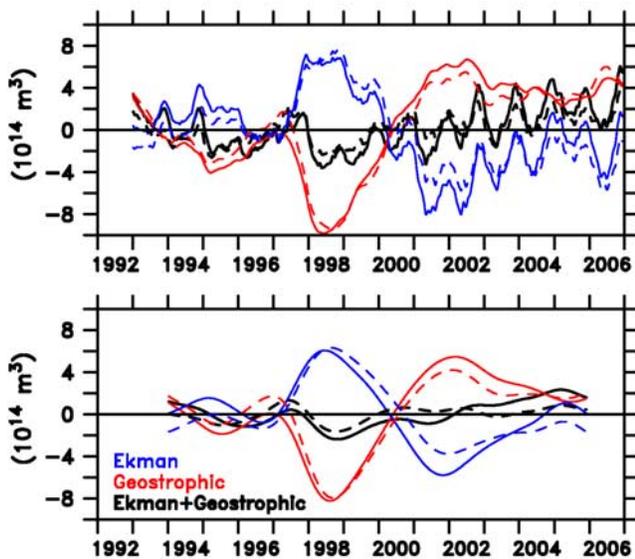
Figure 6. Time series of time integrated meridional (red curves) geostrophic transports, (blue curves) Ekman transports, and (black curves) geostrophic plus Ekman transports entering the 5°N−5°S equatorial box. The full lines represent the transports integrated from 120°E to 80°W, the dashed lines from 150°E to 80°W. The top panel shows weekly values, and the bottom panel shows the interannual variations estimated by filtering the weekly values with a 105-week Hanning filter. The anomalies are relative to the 1993−2006 time period. Units are in 10^{14} m^3.

[20] Looking at the two contributors of the net time-integrated transport, Figure 6 illustrates one basic feature of the meridional circulation in the equatorial band: the com-

peting poleward Ekman and equatorward geostrophic transports (and vice versa). It also indicates that the net time-integrated meridional transports displayed in Figure 5 actually represent a small residual between the geostrophic and opposite Ekman transports. It further reveals that the geostrophic and Ekman transports mostly concern the 150°E−90°W longitudes, with a marginal contribution of the longitudes located west of 150°E and east of 90°W. *Meinen and McPhaden* [2001] computed the 1993−1999 net meridional transports from in situ observations across 8°N and 8°S and also concluded that the largest variability occurs in the ocean interior. *Alory and Delcroix* [2002] analyzing the 1964−1999 modeled transports obtained a comparable result regarding the weak contribution of the westernmost and easternmost longitudes. With this caveat, we now concentrate on the meridional geostrophic transports within 150°E−90°W, a zonal band where our wave decomposition technique is exploitable (see the Appendix).

4.2. Warm Water Volume and Equatorial Waves

[21] To set the context regarding equatorial waves, the longitude-time variations of the 5°N−5°S averaged SLA, first baroclinic equatorial Kelvin and m = 1 Rossby wave contributions to sea level are shown in Figure 7 for the 1992−2006 period. Previous works have already investigated the links between a subset of these SLA, the anomalous wind and SST fields (not shown here), and the related sequential propagations of the equatorial Kelvin and Rossby waves [e.g., *Boulanger and Menkes*, 1999; *McPhaden and Yu*, 1999; *Delcroix et al.*, 2000; *Picaut et al.*, 2002; *Lengaigne et al.*, 2002; *Hackert et al.*, 2007]. The derived analyses mostly focused on: (a) how the *zonal* surface currents associated with the equatorial waves contributed to ENSO events, (b) whether or not the waves were wind forced or reflected at the eastern and/or western boundaries,
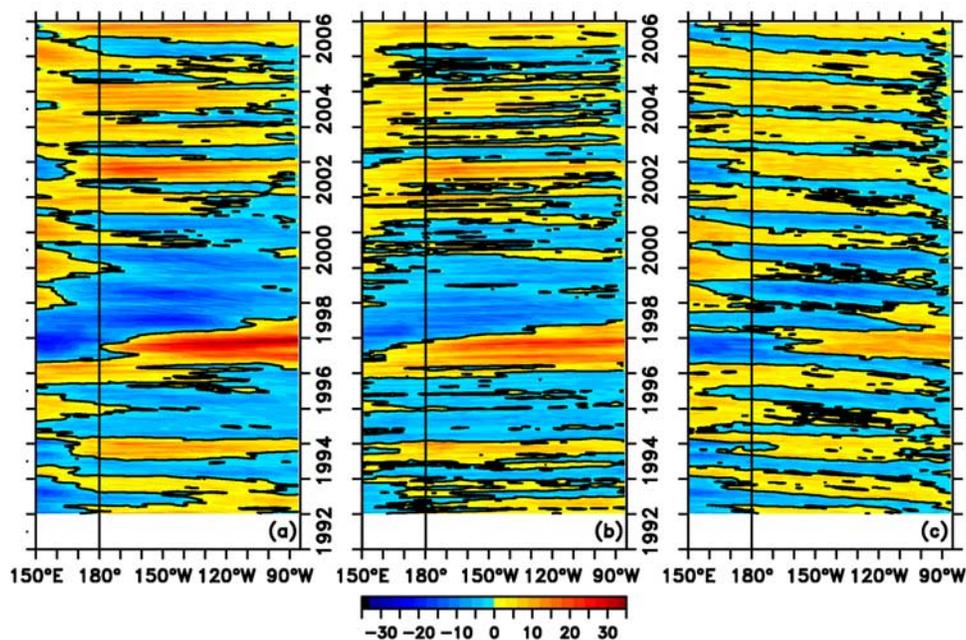
Figure 7. Longitude-time distributions of 5°N−5°S averaged (a) sea level anomalies, (b) first baroclinic Kelvin, and (c) first meridional mode Rossby contribution to the sea level anomalies. Units are in centimeters. The anomalies are relative to the 1993−2006 time period.
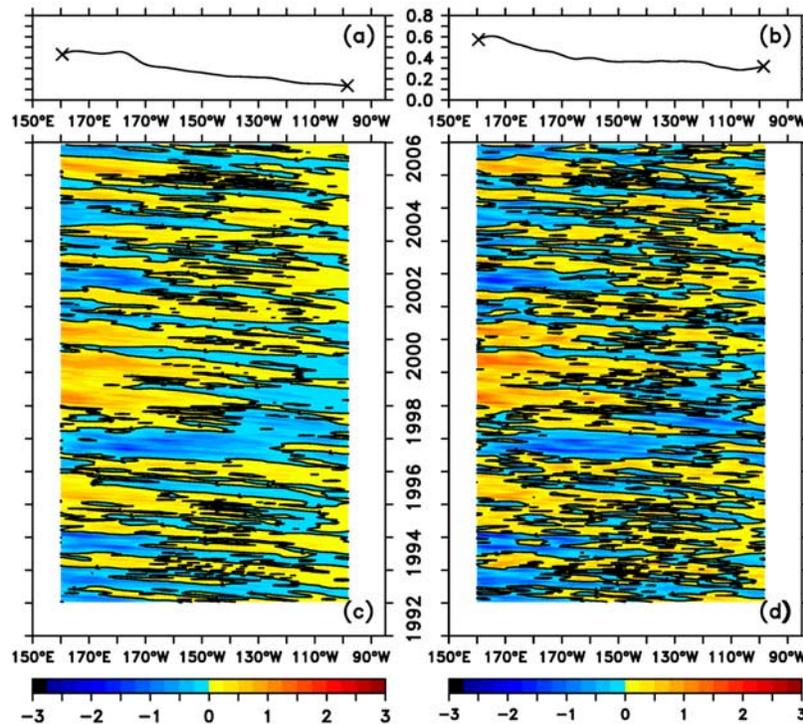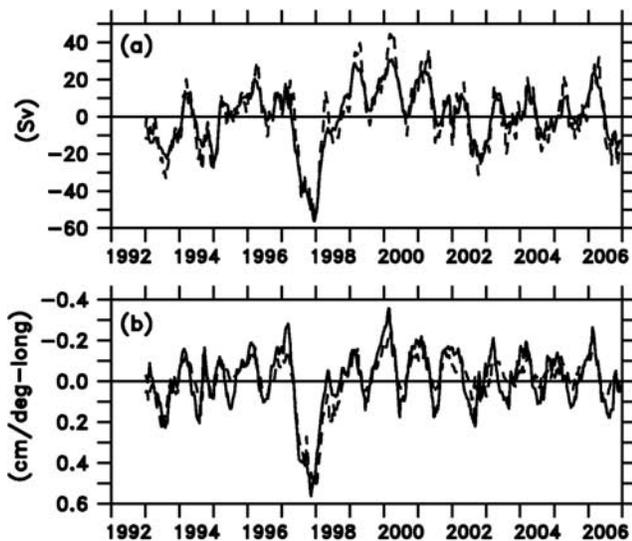
Figure 8. Zonal distribution of the standard deviations of (a) the meridional geostrophic transport anomalies entering the 5°N–5°S equatorial box and (b) the first baroclinic first meridional mode Rossby contribution to this transport. The corresponding longitude-time distributions of the anomalous transports are shown in (c) and (d), respectively. Units are in Sverdrups per degree longitude. The anomalies are relative to the 1993–2006 time period. Note that a 20° longitude Hanning filter was applied for clarity.

and (c) the role of westerly wind bursts and initial conditions for El Niño events to develop. Hence those aspects, some of which being detectable from Figure 7, will not be dealt with here (except the origin of Rossby waves in section 4.3) as they are rather well documented already. Rather, we focus on how the *meridional* surface currents associated with equatorial waves affect the ENSO features via the recharge/discharge of the equatorial band. Of note, it is worth reminding that equatorial Kelvin waves have no meridional current signature ($v = 0$, see the Appendix). The contribution of equatorial Rossby wave only is thus analyzed below.

[22] The longitude-time distribution of the anomalous meridional geostrophic transports of WWV entering the 5°N–5°S equatorial band is shown in Figure 8c. We clearly observe westward propagation during the whole period, with the anomalies crossing the basin in about half a year. The analysis of significant time lag correlations between all the 10°-longitude averaged SLA time series for the central basin (160°E–140°W) yields phase speed of 0.77 ± 0.04 m/s (the second number is one standard deviation). It corresponds to the theoretical phase speed of the first baroclinic m = 1 Rossby wave [$c/(2m + 1)$], with c ranging within 2.3 and 2.8 m/s in this longitudinal band when computed from climatological density profiles [*Picaut and Sombardier*, 1993]. The variability of these transports (Figure 8a) increases westward, with the largest values west of 170°W, meaning that the geostrophic WWV recharge/discharge of the equatorial band mostly occur in the western half of the basin. This westward increase still remains (figure not shown

here) if the sloping thermocline depths along 5°N and 5°S [$\overline{Z}_{20}(x, 5°N)$ and $\overline{Z}_{20}(x, 5°S)$ in equation (5)] involved in the vertical integration of the transports are replaced by a longitudinally constant thermocline depth [$\overline{Z}_{20}(x, 5°N) = \overline{Z}_{20}(x, 5°S) = 100$ m]. Such a test indicates that the transport variability is mostly influenced by the changes of SLA (hence thermocline slope anomaly) rather than of mean thermocline. Interestingly, the transport contribution of the first baroclinic m = 1 Rossby mode (Figures 8c and 8d) is almost identical to the above-noted anomalous transports. The phase speed of the propagation is then 0.84 ± 0.04 m/s. Clearly, Figures 8a–8d indicate that the meridional geostrophic transport anomalies filling up or draining the equatorial band can be fairly well reproduced using only the first baroclinic m = 1 Rossby modes. Besides, the phase speed agreement in Figures 8c–8d justifies a posteriori using the first baroclinic mode phase speed to project the SLA.

[23] The meridional geostrophic transports across the 5°N and 5°S latitudes (again counted positive when directed to the equator), now integrated from 150°E to 90°W, are compared with the contribution of the first baroclinic m = 1 Rossby mode, for the weekly (Figure 9a) and 105-week Hanning filtered (Figure 10) values. Again, it shows that the Rossby mode explains most of the meridional geostrophic transports, accounting for about 88% of the total variance (R = 0.94). It also shows that the discharges of the equatorial band clearly occurred during the 1992–1994 (easily visible in 1994 in Figure 10), 1997–1998 and 2002, 2004, and 2006 (not visible in Figure 10) El Niño events, and the recharges happened conversely during the

Figure 9. (a) Time series of 150°E–80°W meridional geostrophic transports entering the 5°N–5°S equatorial box. The full line represents the transports computed from the Sea Level Anomalies (SLA), and the dashed line from the first baroclinic first meridional mode Rossby contribution. Units are in Sverdrups. (b) Time series of zonal sea level slope anomalies, as estimated by a linear least squares fits of the SLA along 5°N (full line) and 5°S (dashed line) from 150°E to 80°W. Units are centimeters per degree longitude, and the vertical axis increases downward. The anomalies are relative to the 1993–2006 time period.

1996 and 1999–2001 La Niña events. As intuited in section 3, Figure 9a further indicates that warm water discharges (recharges) of the equatorial band tend to be associated with downwelling (upwelling) Rossby waves, showing up as positive (negative) SLA in Figure 7c.

[24] From a physical point of view, the relationships between Rossby Wave propagations and the geostrophic RD of the equatorial band can be understood looking at the zonal SLA slopes along 5°N and 5°S (Figure 9b). These slopes were computed by least squares fitting a straight line to the SLA values within 150°E–80°W along these two latitudes. Remarkably, the westward propagation of downwelling Rossby waves (SLA > 0 in Figure 7c) tends to induce positive SLA slopes along 5°N and 5°S (>0 values in Figure 9b), merely because positive SLA appear first in the East and about half a year later in the West. These positive SLA slopes correspond to a reduced thermocline slopes (see equation (5)), and so result in a poleward geostrophic transport anomaly (<0 values in Figure 9a) given the opposite sign of the Coriolis parameter at 5°N and 5°S. The reverse processes apply for upwelling Rossby Waves (SLA < 0 in Figure 7c) which so induce equatorward geostrophic transport anomaly (>0 values in Figure 9a). In other words, the large-scale structure of the equatorial Rossby waves affects the basin-scale zonal slope of the thermocline and, as a consequence, the related meridional geostrophic current convergences that impinge on the geostrophic RD of the equatorial band. Another remarkable feature appears in Figure 10. It shows that the geostrophic

RD of the equatorial band, tightly linked to equatorial Rossby waves, is proportional and in phase opposition with the anomalous NIÑO3.4 SST. This is one of the reasons why the time-integrated geostrophic RD, in phase with the WWV (Figure 6), precedes the anomalous NINO3.4 SST.

4.3. Generation of Equatorial Rossby Waves

[25] It is instructive at this point to discuss the likely generation mechanisms of the equatorial Rossby waves. This has been done in several previous studies, for time periods different than our, in using either GEOSAT or TOPEX/ Poseidon altimeter data, in situ TAO mooring data and/or numerical models (linear and OGCM). A partial review of the pre-2000 studies is given by *Delcroix et al.* [2000, their section 4]. As a complement to these previous studies, with the data we have in hand and for the 1992–2006 period, we simply compare time series of zonal wind anomalies in equatorial boxes with time series of first baroclinic m = 1 Rossby wave contribution to SLA in other equatorial boxes located few degrees longitude to the west (that is away from the assumed forcing region). Note that the projection of the zonal wind onto the m = 1 Rossby is equivalent to the zonal wind itself, although with opposite sign and about half the amplitude [see *Wakata and Sarachik, 1991*]. Figure 11 shows the zonal distribution of the lagged correlation coefficients between the zonal wind anomalies, averaged in 5°N–5°S and 20° longitude moving boxes, versus the m = 1 Rossby wave contribution to SLA, averaged in boxes of similar sizes centered 30° longitude to the west. (Note that choosing boxes of 10° to 30° longitude does not change the results significantly). The maximum correlations between the time series clearly appear west of about 130°W, with a sharp decrease of the correlations in the eastern basin. West of about 130°W, the best correlations (of the order of −0.8) are obtained generally when the zonal wind leads the Rossby wave signal by 4 to 8 weeks (1 to 2 months), consistent with the transit time of Rossby waves between the two equatorial boxes (30° longitude in 4 to 8 weeks yields phase speeds of 1.4 to 0.7 m/s, respectively).

[26] This simple calculation suggests that, in general, Rossby waves west of about 130°W owe their existence to the wind-forcing, whereas those east of about 130°W originate mostly from eastern boundary reflection. In agreement with these findings, sensitivity studies with simple
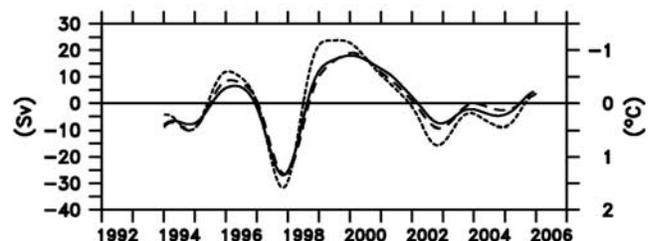
Figure 10. (full and long-dashed lines) Same as Figure 9a for the interannual variations estimated by filtering the weekly values in with a 105-week Hanning filter. Units are in Sverdrups scaled on the left vertical axis. (short-dashed line) Time series of interannual variations of NIÑO3.4 SST anomalies. Units are in Celsius scaled on the right vertical axis which increases downward. The anomalies are relative to the 1993–2006 time period.
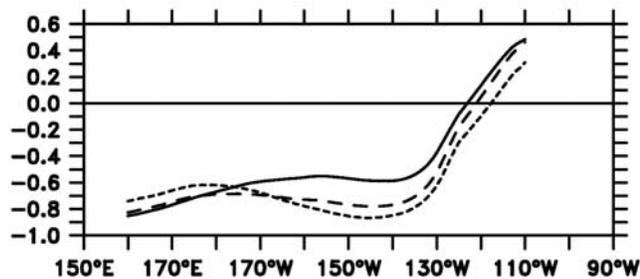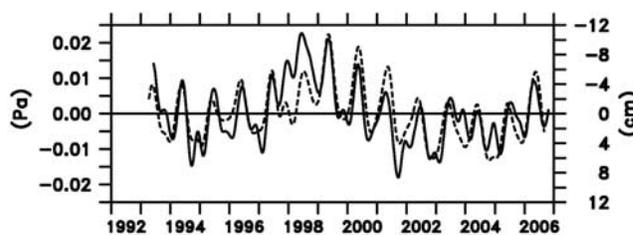
Figure 11. Correlation coefficients between 27-week Hanning filter zonal wind anomalies, averaged in 5°N–5°S and 20° longitude moving boxes, versus the Rossby wave contribution to Sea Level Anomalies (SLA), averaged in similar boxes centered 30° longitude to the west. Correlations are computed when the zonal wind leads the Rossby wave signal by (full line) 0, (long dashed line) 4 and (short dashed line) 8 weeks. Only correlations in excess of ±0.6 are significant at the 95% confidence level. The longitudes ascribed to the correlations denote the centers of the SLA boxes.

linear models, forced with and without Rossby forcing, indicate that the wind (eastern boundary reflection) is actually responsible for the propagation of Rossby waves in the western (eastern) half of the equatorial Pacific basin during 1992–1998 [see *Delcroix et al.*, 2000, plate 3]. Besides, a dedicated study aiming to unravel the respective contribution of wind-forcing and eastern boundary reflection for Rossby waves in the eastern Pacific, as was conducted by *Boulanger et al.* [2003] for Kelvin waves in the western Pacific, concluded that eastern boundary reflection accounts for less than 30% of the Rossby wave SLA variance at 125°W [S. Cravatte, personal communication, 2007].

[27] The effects of wind-forcing and boundary reflection processes are obviously not mutually exclusive, especially in the eastern half of the Pacific basin. As an example, their interplay can be suspected in Figure 12 that compares time series of zonal wind anomaly in the eastern-central equatorial Pacific (5°N–5°S, 120°W–140°W) with time series of Rossby Wave signal in the western-central equatorial Pacific (5°N–5°S, 150°W–170°W). Overall, there is an excellent agreement between the two time series (R = −0.77 for a lag of 2 months); the largest differences occurred during the 1997–1998 El Niño when the downwelling Rossby waves in the eastern half of the basin appear to be reflected from the downwelling Kelvin waves reaching the eastern coast by the end of 1997 (see Figures 7b and 7c). As noted earlier by *Delcroix et al.* [2000], based on their literature review, it is thus not realistic to devise a single response regarding the contributions of wind-forcing and eastern boundary reflections for a given time period.
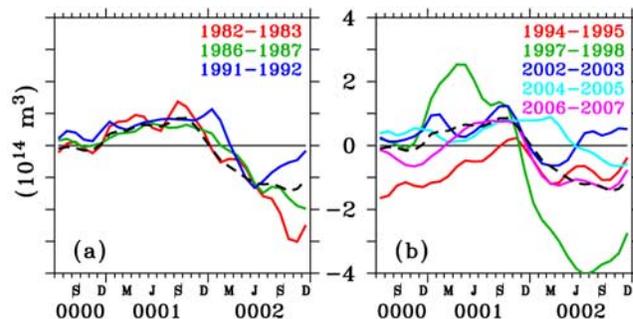
4.4. Comparison Between ENSO Episodes

[28] In addition to analyzing common features, many previous studies have documented the dissimilarity of the ENSO events of the last decades. The events have so been classified according to surface and, to a less extent, subsurface criteria. Regarding the surface, ENSO events were catalogued depending on: the strength, duration, onset and/

or termination time of significant SST anomalies in given spatial boxes (NIÑO3, NIÑO3.4, etc.), patterns of zonal SST gradients, eastward versus westward propagation of SST anomalies along the equator, location of maximum SST anomaly, and/or phasing agreement with the mean seasonal cycle [e.g., *Rasmusson and Carpenter*, 1982; *Fu et al.*, 1986; *Wang*, 1995; *Wang and Picaut*, 2004; *Trenberth and Stepaniak*, 2001; *Xu and Chan*, 2001; *Lengaigne et al.*, 2006; *Ashok et al.*, 2007]. Such classifications were also carried out from modern and projected SST simulations [e.g., *Cabos Narvaez et al.*, 2006; *Guilyardi*, 2006; *Leloup et al.*, 2007].

[29] Very few classification efforts were conducted relying on subsurface criteria. These mostly consider heat content anomalies, an alias for WWV, their timing, the speed of the eastward propagation, and/or the link with SST anomalies [*Xu and Chan*, 2001; *Hasegawa et al.*, 2006]. To complement these studies, Figure 13 compares the WWV

Figure 12. Times series of (full line) zonal wind anomalies averaged in the eastern-central equatorial Pacific (5°N–5°S, 120°W–140°W), and (dashed line) first baroclinic m = 1 Rossby mode contribution to Sea Level Anomalies (SLA) averaged in the western-central equatorial Pacific (5°N–5°S, 150°W–170°W) and lagged by 2 months. Units are in Pascal and centimeters, respectively. The anomalies are relative to the 1993–2006 time period. Note that a 27-week (about 3 months) Hanning filter was applied on each time series for clarity, the y axis increases downward for SLA, and positive values denote westerly wind.

Figure 13. Time series of Warm Water Volume (WWV) anomalies for eight El Niño episodes. The curves on (a) are derived form in situ observations, and on (b) from equivalent Sea Level Anomalies (SLA) measurements (see Figure 2 for a comparison). Years 0001 on the time axis are 1982, 1986, 1991, 1994, 1997, 2002, 2004, and 2006. The dashed black lines on both panels are the average of the eight El Niño episodes. The anomalies are relative to the mean seasonal cycle of WWV computed over the 1993–2006 time period excluding 1997–1998. Units are in 10^{14} m^3.
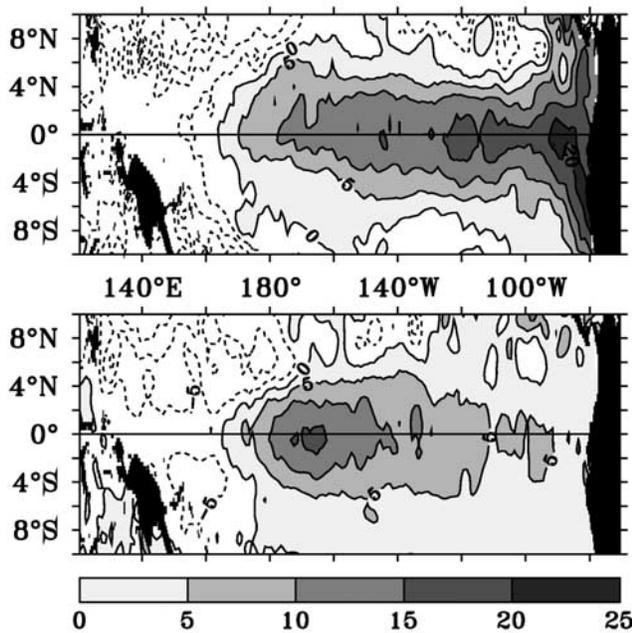
Figure 14. Spatial distribution of three-month averaged sea level anomalies (an alias for Warm Water Volume, see Figure 2) centered on (a) May 1997 and (b) September 2002, at times of maximum WWV changes associated with the 1997–98 and 2002 El Niño events, respectively. Units are in centimeters.

anomaly time series for the eight El Niño episodes of the 1980–2007 time period. Three El Niño episodes occurred during the first half of that period (Figure 13a). Their WWV amplitude is similar; the positive WWV anomalies lasted for about one year and reached maximum values by the end of El Niño years. Overall, the three WWV time series are rather indistinguishable and resemble rather well the mean time series, even for the 1982–1983 El Niño considered as "very strong" based on other criteria. Five El Niño episodes occurred during the second half of the period (Figure 13b), suggesting a trend toward more frequent El Niño in recent years. Then, the dispersion about the WWV mean time series is much larger, and the specificity of the 1997–1998 El Niño clearly shows up. Only for that last episode was a rapid rise in WWV during the preceding winter of the El Niño year, and a maximum WWV in boreal spring. Still, the spatial distribution of WWV for the 1997–1998 El Niño also differs from the other El Niño events. In 1997–1998, the maximum WWV anomaly appears in the eastern and central equatorial basin (Figure 14a). In contrast, for the other events, the maximum WWV was chiefly trapped to the equator in the central basin only, as exemplified for the 2002 El Niño (Figure 14b).

[30] It is interesting to note that the lag of 2–3 seasons between WWV and NIÑO3.4 SST for the 1997–1998 El Niño event seems to reduce to 1–2 seasons for the following events (Figure 1) [see also *McPhaden*, 2008]. Two possible elements may be related to this possible lag change. First, the 1997–1998 events occurred during a phase of positive Trans Niño (TNI) and negative El Niño Modoki (EMI) indices [*Trenberth and Stepaniak*, 2001;

Ashok et al., 2007]. This contrasts with the post 1997–1998 events which happened during a phase of opposite signs in TNI and EMI during which the maximum SST anomalies are located in the central rather than in the eastern equatorial basin. Secondly, the activity of equatorial Rossby waves was enhanced after the 1997–1998 El Niño event (Figure 7c), resulting in the dominance of geostrophic over Ekman meridional transports of WWV (Figure 6). Whether or not this is fortuitous cannot be decided with the 1992–2006 data we have in hand. The analysis of a longer time period will be necessary to draw further conclusions on this issue.

5. Conclusion and Discussion

[31] As reviewed by *Wang and Picaut* [2004], the quasi cyclic nature of ENSO is presently accounted for by four major theories. These include the RD oscillator theory which, in particular, put emphasis on ENSO-related WWV transfers between the equatorial and off-equatorial regions. To make further progress in better understanding those meridional transfers, we focus on the mechanisms responsible for the observed equatorial WWV changes which are critical for ENSO development and prediction ([*Wyrtki*, 1985; *Zebiak and Cane*, 1987]; see also the references in section 1). In line with previous results which are reviewed, we demonstrated that the equatorial (5°N–5°S) WWV changes during 1992–2006 can be derived from the areal integral of sea level anomalies (SLA) obtained from altimeter measurements. For the study period, we evidence WWV discharges of the equatorial band during the 1992–1994, 1997–1998, 2002, 2004, and 2006 El Niño events, and WWV recharges during the 1996 and 1999–2001 La Niña events.

[32] The role of the geostrophic and Ekman transports in the ENSO-related equatorial WWV changes was then investigated. The geostrophic transports above the thermocline were estimated from SLA only, and validated against in situ transports obtained at different locations. Ekman transports were derived using wind data. We demonstrated that the equatorial WWV changes result from the residual effects of converging geostrophic and diverging Ekman meridional transports (or vice versa). Interestingly, we showed that changes of the meridional geostrophic transports largely result from the westward propagation of wind-forced first baroclinic and first meridional (m = 1) mode equatorial Rossby waves which induce changes in the zonal slope of the thermocline. View from the ocean side of a coupled ocean-atmosphere problem, the zonal wind-forcing thus has two effects: first, it drives Ekman transport, and second, it initiates equatorial Rossby waves, which all together combine to change the equatorial WWV. The role of equatorial Rossby waves on the meridional redistribution involved in the RD of the equatorial band was referred to by *Zebiak and Cane* [1987], *Springer et al.* [1990], *Jin* [1997], *An and Kang* [2000], and *Meinen and McPhaden* [2001]. To our knowledge, it is the first time with this paper that this is established with observational data.

[33] As reminded in the Introduction, previously published EOF analyses of SLA (or proxies such as upper layer heat content, thermocline depth or surface dynamic height) have evidenced two main statistically derived modes of

ENSO variability: a zonal seesaw pattern in the equatorial band, and a meridional seesaw pattern between the equatorial and off-equatorial regions. These are not rigid seesaws [e.g., see *Delcroix*, 1998, Figures 4c–4d]. Actually, they reflect the influence of propagating equatorial waves which induce, on one hand, a zonal redistribution of warm water mainly due to zonal advection [e.g., *Picaut and Delcroix*, 1995] which induce changes in the zonal tilt of the thermocline and, on the other hand, a meridional redistribution of warm water due to changes in the related zonal pressure gradient which products anomalous meridional convergence (or divergence). While the zonal redistribution of warm water is known as *the* canonical ENSO feature, it should be kept in mind that it is the meridional redistribution which yields to changes in the zonal mean thermocline depth, a necessary condition for ENSO to oscillate in a coupled model [*Zebiak and Cane*, 1987], and a possible cause of apparent changes in ENSO properties [*Fedorov and Philander*, 2000].

[34] The above results have some obvious limitations and raise interesting questions. First, our meridional geostrophic transport changes were estimated in using a gridded SLA field which actually does not extent all the way to the eastern and western Pacific coasts. This may induce errors in the transports, especially in the gappy western boundary of the equatorial Pacific Ocean where sporadic in situ observations had revealed very energetic regional currents [*Lindstrom et al.*, 1990; *Ridgway et al.*, 1993]. We can anticipate the upcoming SPICE program (Southwest Pacific Ocean Circulation and Climate Experiment [*Ganachaud et al.*, 2007]), at least, will help us to quantify these energetic western boundary current contributions to the WWV changes of the equatorial band. Secondly, our wave decomposition technique did not allow us to compute the Rossby wave contributions to the meridional Geostrophic transports west of 150°E, due to the presence of the Papua New Guinea coast near the equator. While we showed these western transports to be likely unimportant (at least from 150°E to the westernmost gridded point in SLA; Figure 6), it would be interesting to confirm that result in testing other decomposition techniques such as those applicable near coastal regions of the western equatorial Pacific [*Boulanger and Menkes*, 1999] or Guinea Gulf in the eastern equatorial Atlantic [*Illig et al.*, 2004]. Thirdly, to investigate the role of equatorial first baroclinic m = 1 Rossby waves, we projected the SLA onto a theoretical latitudinal structure which is symmetrical about the equator (see the Appendix). In doing this, we therefore imposed the meridional geostrophic transports related to Rossby waves to be the same amplitude (and opposite sign) at 5°N and 5°S. The use of a theoretical asymmetric, rather than symmetric, latitudinal structure could actually be more appropriate given the effects of the meridional shears in the mean equatorial current system [*Chelton et al.*, 2003]. In that case, we would expect a much larger meridional geostrophic transports at 5°N than at 5°S (Ibid, their Figure 19). Such asymmetric feature would be more coherent with some observations (see Section 1) which evidence the meridional WWV changes to chiefly occur between the regions north and south of about 5°N. An alternative explanation for the asymmetry of the observed WWV changes is the asymmetry of the wind field which impacts both the Ekman and geostrophic transports [*Kug et*

al., 2003]. Clearly, the spatial asymmetry in the WWV changes is worth to be further analyzed. Fourthly, we did not analyze the possible contributions of higher order baroclinic modes to the meridional geostrophic transports. Analysis of zonal SLA propagations and equatorial trapping scale independently indicates that SLA changes are strongly dominated by the first baroclinic mode [*Delcroix et al.*, 1991, Figure 7]. Notwithstanding, it would be interesting to assess the higher mode contributions with simple linear models or assimilation products which have proven quite realistic at simulating SLA and currents [e.g., *Delcroix et al.*, 2000; *Dewitte et al.*, 2003]. The use of linear models will further allow us to analyze a time period longer than the 1992–2006 one used here, to test possible changes in the ENSO-related WWV characteristics before and after the mid-1970s [*An et al.*, 2006], as well as the hint for recent changes in the relation between WWV and NIÑO3.4 SST that we suggest may result from enhanced Rossby Wave activity. Besides, such linear models will help us to re-examine the actual role of the wind-forcing and Kelvin wave reflection in Rossby Wave generation and derived WWV changes. Finally, the behavior of the ENSO-related WWV changes must be evaluated and compared in Coupled General Circulation Models (CGCM), as was done for other ENSO features [e.g., *Delecluse et al.*, 1998; *Guilyardi*, 2006]. The IPCC AR4 (Intergovernmental Panel on Climate Change Fourth Assessment Report) coupled GCMs are good candidates for such an investigation although they may misrepresent the western boundary current transport due to their rather coarse resolution. The present analysis, based on in situ and remote observations, tells us about WWV in the real world during a limited (and maybe specific) time period: it is clearly one step of a longer work presently under consideration.

Appendix A

[35] The respective contribution of the first baroclinic Kelvin (M) and Rossby (R) modes to the sea level (h) and zonal current (u) anomalies was computed following *Cane and Sarachik* [1981] and the method detailed by *Delcroix et al.* [1994]. This method consists in projecting the signal onto the theoretical meridional structures in sea level (h) and zonal surface current (u), so that:

$$\begin{bmatrix} u \\ h \end{bmatrix} = a_K(x,t)\vec{M}_{-1}(y) + \sum_{m>0} a_{R,m}(x,t)\vec{R}_m(y)$$

with $\vec{M}_{-1}(y) = \dfrac{1}{\sqrt{2}}\begin{bmatrix} \psi_0 \\ \psi_0 \end{bmatrix}$ and $\vec{R}_m(y) = \dfrac{1}{2\sqrt{2}}\begin{bmatrix} \dfrac{\psi_{m+1}}{\sqrt{m+1}} - \dfrac{\psi_{m-1}}{\sqrt{m}} \\ \dfrac{\psi_{m+1}}{\sqrt{m+1}} - \dfrac{\psi_{m-1}}{\sqrt{m}} \end{bmatrix}$

where the ψ_n are derived from the Hermite polynomials. Noting that the Kelvin mode has no meridional current signature ($v = 0$) and the ψ_n forming an orthogonal base, the contribution of the Rossby modes to the meridional current anomalies is then obtained from:

$$v_m(x,y,t) = \frac{1}{2m+1}\frac{\partial a_{R,m}}{\partial x}\psi_m(y)$$
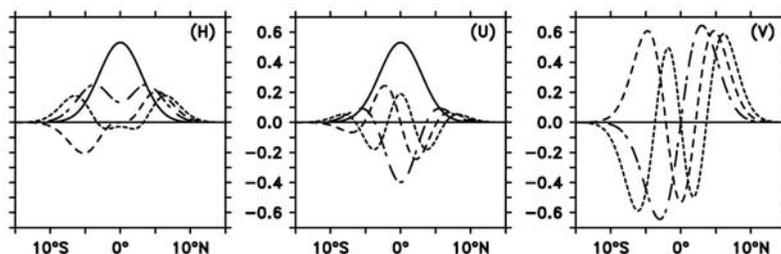
Figure A1. Theoretical meridional distributions of normalized amplitudes in Kelvin modes (solid lines), first (dash-dotted lines), second (long dashed lines), and third (short dashed lines) meridional Rossby modes for sea level (H), zonal (U) and meridional (V) currents. The horizontal scale has been converted in physical unit (degree latitude) in using a first baroclinic mode phase speed c = 2.8 m/s.

[36] The theoretical meridional structures of the Kelvin (K), and first three Rossby (R1, R2, R3) modes to h, u and the meridional (v) surface currents are shown in Figure A1, in using a first baroclinic mode phase speed c = 2.8 m s^{-1} representative of the western equatorial Pacific Ocean [*Picaut and Sombardier*, 1993]. Noteworthy, with the method discussed by *Delcroix et al.* [1994], the contribution of these modes cannot be quantified west of 150°E due to the presence of the Papua New Guinea coast near the equator, which prohibits a reliable calculation [see *Boulanger and Menkes* [1995] and *Illig et al.* [2004] for alternate methods].

[37] The contribution of equatorial waves to the current transports was then estimated by fitting a third order polynomial to a mean vertical velocity profile representing the average of 13 first baroclinic mode theoretical profiles (Figure A2), as derived from Brunt Vaisälä frequencies [see *Eriksen*, 1982] computed every 10° longitude along the equator from an OGCM ORCA model output [see *Cravatte et al.*, 2003]. Such a mean theoretical profile has proven reasonable as compared to sporadic current observations in the western equatorial Pacific [*Delcroix et al.*, 1992, Figure 18b].

References

Alory, G., and T. Delcroix (2002), Interannual sea level changes and associated mass transports in the tropical Pacific from TOPEX/Poseidon data and linear model results (1964–1999), *J. Geophys. Res.*, *107*(C10), 3153, doi:10.1029/2001JC001067.

An, S. I., and I. S. Kang (2000), A further investigation of the recharge oscillator paradigm for ENSO using a simple coupled model with the zonal mean and eddy separated, *J. Clim.*, *13*, 1987–1993.

An, S.-I., Z. Ye, and W. W. Hsieh (2006), Changes in the leading ENSO modes associated with the late 1970s climate shift: Role of surface zonal current, *Geophys. Res. Lett.*, *33*, L14609, doi:10.1029/2006GL026604.

Ashok, K., S. K. Behera, S. A. Rao, H. Weng, and T. Yamagata (2007), El Niño Modoki and its possible teleconnection, *J. Geophys. Res.*, *112*, C11007, doi:10.1029/2006JC003798.

Bentamy, A., P. Queffeulou, Y. Quilfen, and K. Katsaros (1999), Ocean surface wind fields estimated from satellite active and passive microwave instruments, *IEEE Trans. Geosci. Remote Sens.*, *37*, 2469–2486.

Bjerknes, J. (1969), Atmospheric teleconnections from the equatorial Pacific, *Mon. Weather Rev.*, *97*, 163–172.

Boulanger, J.-P., and C. Menkes (1995), Propagation and reflection of long equatorial waves in the Pacific Ocean during the 1992–1993 El Niño, *J. Geophys. Res.*, *100*(C12), 25,041–25,059.

Boulanger, J. P., and C. Menkes (1999), Long equatorial wave reflection in the Pacific Ocean from TOPEX/POSEIDON data during the 1992–1998 period, *Clim. Dyn.*, *15*, 205–225.

Boulanger, J. P., S. Cravatte, and C. Menkes (2003), Reflected and locally wind-forced interannual equatorial Kelvin waves in the western Pacific Ocean, *J. Geophys. Res.*, *108*(C10), 3311, doi:10.1029/2002JC001760.

Cabos Narvaez, W., F. Alvarez-Garcia, and M. J. OrtizBeviá (2006), Impact of global warming on ENSO phase change, *Adv. Geosci.*, *6*, 103–110.

Cane, M. A., and E. S. Sarachik (1981), The response of a linear baroclinic equatorial ocean to periodic forcing, *J. Mar. Res.*, *39*, 651–693.

Chelton, D. B., M. G. Schlax, J. M. Lyman, and G. C. Johnson (2003), Equatorially trapped Rossby waves in the presence of meridionally sheared baroclinic flow in the Pacific Ocean, *Prog. Oceanogr.*, *56*, 323–380.

Cibot, C., E. Maisonnave, L. Terray, and B. Dewitte (2005), Mechanisms of tropical Pacific interannual-to-decadal variability in the Arpege/Orca global coupled model, *Clim. Dyn.*, *24*(8), 823–842.
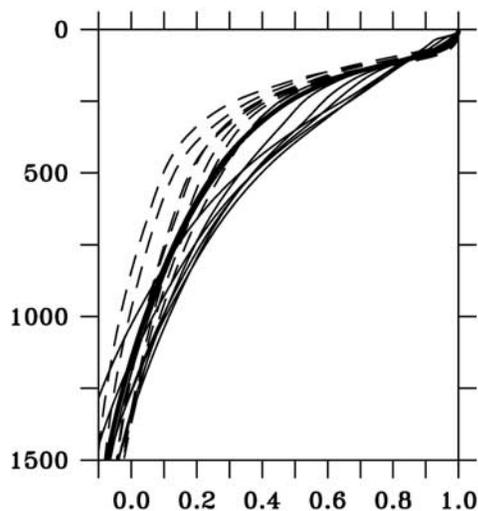
Figure A2. Normalized vertical distribution of the first baroclinic mode horizontal velocity, as derived from Brunt Vaïssala frequencies computed every 10° longitude along the equator. The dashed lines are for longitudes west of 150°W, and the thin full lines east of 150°W. The heavy black line is the mean vertical profile (see the Appendix for details).

Clarke, A. J., and S. Van Gorder (2001), ENSO prediction using an ENSO trigger and a proxy for western equatorial Pacific warm pool movement, *Geophys. Res. Lett.*, *28*(4), 579–582.

Clarke, A. J., S. Van Gorder, and G. Colantuono (2007), Wind stress curl and ENSO discharge/recharge in the equatorial Pacific, *J. Phys. Oceanogr.*, *37*, 1077–1091, doi:10.1175/JPO3035.1.

Cravatte, S., J. Picaut, and G. Eldin (2003), Second and first baroclinic Kelvin modes in the equatorial Pacific at intraseasonal timescales, *J. Geophys. Res.*, *108*(C8), 3266, doi:10.1029/2002JC001511.

Delcroix, T. (1998), Observed surface oceanic and atmospheric variability in the tropical Pacific at seasonal and ENSO timescales: A tentative overview, *J. Geophys. Res.*, *103*(C9), 18,611–18,634.

Delcroix, T., and G. Eldin (1995), *Observations hydrologiques dans l'Océan Pacifique Tropical Ouest*, Campagnes SURTROPAC 1 à 17, de janvier 1984 à août 1992, campagnes COARE156 1 à 3, d'août 1991 à octobre 1992, Travaux et Documents Microfichés, vol. 141, 78 pp., ORSTOM Editions, Paris.

Delcroix, T., and J. Picaut (1998), Zonal displacement of the western equatorial Pacific "fresh pool", *J. Geophys. Res.*, *103*(C1), 1087–1098.

Delcroix, T., J. Picaut, and G. Eldin (1991), Equatorial Kelvin and Rossby Waves evidenced in the Pacific Ocean through GEOSAT sea level and surface current anomaly, *J. Geophys. Res.*, *96*(Suppl.), 3249–3269.

Delcroix, T., G. Eldin, M.-H. Radenac, J. Toole, and E. Firing (1992), Variation of the western equatorial Pacific Ocean, 1986–1988, *J. Geophys. Res.*, *97*(C4), 5423–5445.

Delcroix, T., J.-P. Boulanger, F. Masia, and C. Menkes (1994), Geosat-derived sea level and surface current anomalies in the equatorial Pacific during the 1986–1989 El Niño and La Niña, *J. Geophys. Res.*, *99*(C12), 25,093–25,107.

Delcroix, T., B. Dewitte, Y. duPenhoat, F. Masia, and J. Picaut (2000), Equatorial waves and warm pool displacements during the 1992–1998 El Niño Southern Oscillation events: Observation and modeling, *J. Geophys. Res.*, *105*(C11), 26,045–26,062.

Delecluse, P., M. Davey, Y. Kitamura, S. Philander, M. Suarez, and L. Bengtsson (1998), Coupled general circulation modeling of the tropical Pacific, *J. Geophys. Res.*, *103*(C7), 14,357–14,373.

Dewitte, B., S. Illig, L. Parent, Y. duPenhoat, L. Gourdeau, and J. Verron (2003), Tropical Pacific baroclinic mode contribution and associated long waves for the 1994–1999 period from an assimilation experiment with altimetric data, *J. Geophys. Res.*, *108*(C4), 3121, doi:10.1029/2002JC001362.

Ducet, N., P. Le Traon, and G. Reverdin (2000), Global high-resolution mapping of ocean circulation from TOPEX/Poseidon and ERS-1 and -2, *J. Geophys. Res.*, *105*(C8), 19,477–19,498.

Durand, F., and T. Delcroix (2000), On the variability of the tropical Pacific thermal structure during the 1979–96 period, as deduced from XBT sections, *J. Phys. Oceanogr.*, *30*, 3261–3269.

Emery, W. J., and R. E. Thomson (1998), *Data and Their Analysis Methods in Physical Oceanography*, 634 pp., Pergamon Press, Amsterdam.

Eriksen, C. (1982), Equatorial wave vertical modes observed in a western Pacific island array, *J. Phys. Oceanogr.*, *12*, 1206–1227.

Fedorov, A. V., and S. G. H. Philander (2000), Is El Niño changing?, *Science*, *228*(5473), 1997–2002.

Fu, C., H. F. Diaz, and J. O. Fletcher (1986), Characteristics of the response of sea surface temperature in the central Pacific associated with warm episodes of the Southern Oscillation, *Mon. Weather Rev.*, *114*, 1716–1738.

Ganachaud, A., et al. (2007), *Southwest Pacific Ocean Circulation and Climate Experiment (SPICE). Part I: Scientific Background*, International CLIVAR Project Office, CLIVAR Publication Series No. 111, Project Office NOAA OAR Special Report, 37 pp., NOAA/OAR/PMEL, Seattle, WA.

Glantz, M. H. (1996), *Currents of Change*, p. 194, Cambridge Univ. Press, New York.

Goddard, L., and M. Dilley (2005), El Niño: Catastrophe or opportunity, *J. Clim.*, *18*, 651–665, doi:10.1175/JCLI-3277.1.

Guilyardi, E. (2006), El Niño–mean state–seasonal cycle interactions in a multimodel ensemble, *Clim. Dyn.*, *26*, 329–348.

Hackert, E., J. Ballabrera-Poy, A. J. Busalacchi, R.-H. Zhang, and R. Murtugudde (2007), Comparison between 1997 and 2002 El Niño events: Role of initial state versus forcing, *J. Geophys. Res.*, *112*, C01005, doi:10.1029/2006JC003724.

Hasegawa, T., and K. Hanawa (2003), Decadal-scale variability of upper ocean heat content in the tropical Pacific, *Geophys. Res. Lett.*, *30*(6), 1272, doi:10.1029/2002GL016843.

Hasegawa, T., T. Horii, and K. Hanawa (2006), Two different features of discharge of equatorial upper ocean heat content related to El Niño events, *Geophys. Res. Lett.*, *33*, L02609, doi:10.1029/2005GL024832.

Holland, C. L., and G. T. Mitchum (2003), Interannual volume variability in the tropical Pacific, *J. Geophys. Res.*, *108*(C11), 3369, doi:10.1029/2003JC001835.

Illig, S., B. Dewitte, N. Ayoub, Y. du Penhoat, G. Reverdin, P. de Mey, F. Bonjean, and G. Lagerloef (2004), Interannual long equatorial waves in the tropical Atlantic from a high-resolution ocean general circulation model experiment in 1981–2000, *J. Geophys. Res.*, *109*, C02022, doi:10.1029/2003JC001771.

Jin, F. F. (1997), An equatorial ocean recharge paradigm for ENSO. part I: Conceptual model, *J. Atmos. Sci.*, *54*, 811–829.

Kirtman, B. P., J. Shukla, J. Balmaseda, N. Graham, C. Penland, Y. Xue, and S. Zebiak (2001), *Current Status of ENSO Forecast Skill: A Report to the CLIVAR Working Group on Seasonal to Interannual Prediction*, *ICPO Publ. Ser.*, vol. 56, 24 pp., International Project Office, Southampton, U.K.

Kug, J.-S., I.-S. Kang, and S.-I. An (2003), Symmetric and antisymmetric mass exchanges between the equatorial and off-equatorial Pacific associated with ENSO, *J. Geophys. Res.*, *108*(C8), 3284, doi:10.1029/2002JC001671.

Leloup, J., M. Lengaigne, and J.-P. Boulanger (2007), Twentieth century ENSO characteristics in the IPCC database, *Clim. Dyn.*, doi:10.1007/s00382-007-0284-3.

Lengaigne, M., J. P. Boulanger, C. Menkes, and H. Spencer (2006), Influence of the seasonal cycle on the termination of El Niño events in a coupled general circulation model, *J. Clim.*, *19*, 1850–1868.

Lengaigne, M., J. P. Boulanger, C. Menkes, S. Masson, P. Delecluse, and G. Madec (2002), Ocean response to the March 1997 westerly wind event, *J. Geophys. Res.*, *107*(C12), 8015, doi:10.1029/2001JC000841.

Lindstrom, E., J. Butt, R. Lukas, and S. Godfrey (1990), The flow through Vitiaz Strait and St. George's Channel, Papua New Guinea, in *The Physical Oceanography of Sea Straits*, pp. 171–189, Springer, New York.

McPhaden, M. J. (1995), The tropical atmosphere ocean array is completed, *Bull. Am. Meteorol. Soc.*, *76*, 739–741.

McPhaden, M. J. (2008), Evolution of the 2006–07 El Niño; The role of intraseasonal to interannual time scale dynamics, *Adv. Geosci.*, *14*, 219–230.

McPhaden, M. J., and X. Yu (1999), Equatorial waves and the 1997–98 El Niño, *Geophys. Res. Lett.*, *26*(19), 2961–2964.

McPhaden, M. J., S. E. Zebiak, and M. H. Glantz (2006a), ENSO as an integrating concept in Earth science, *Science*, *314*, 1740–1745.

McPhaden, M. J., X. Zhang, H. H. Hendon, and M. C. Wheeler (2006b), Large scale dynamics and MJO forcing of ENSO variability, *Geophys. Res. Lett.*, *33*, L16702, doi:10.1029/2006GL026786.

Meinen, C. S. (2005), Meridional extent and interannual variability of the Pacific Ocean tropical-subtropical warm water exchange, *J. Phys. Oceanogr.*, *35*, 323–335, doi:10.1175/JPO-2694.1.

Meinen, C. S., and M. J. McPhaden (2000), Observations of warm water volume changes in the equatorial Pacific and their relationship to El Niño and La Nina, *J. Clim.*, *13*, 3551–3559.

Meinen, C. S., and M. J. McPhaden (2001), Interannual variability in warm water volume transports in the equatorial Pacific during 1993–99, *J. Phys. Oceanogr.*, *31*, 1324–1345.

Miller, L., and R. Cheney (1990), Large-scale meridional transport in the tropical Pacific Ocean during the 1986–1987 El Niño from Geosat, *J. Geophys. Res.*, *95*(C10), 17,905–17,919.

Philander, S. G. (1990), *El Niño, La Niña, and the Southern Oscillation*, p. 293, Elsevier, New York.

Picaut, J., and T. Delcroix (1995), Equatorial wave sequence associated with warm pool displacements during the 1986–1989 El Niño-La Niña, *J. Geophys. Res.*, *100*(C9), 18,393–18,408.

Picaut, J., and L. Sombardier (1993), Influence of density stratification and bottom depth on vertical mode structure functions in the tropical Pacific, *J. Geophys. Res.*, *98*(C8), 14,727–14,737.

Picaut, J., and R. Tournier (1991), Monitoring the 1979–1985 equatorial Pacific current transports with expendable bathythermograph data, *J. Geophys. Res.*, *96*, 3263–3277.

Picaut, J., F. Masia, and Y. duPenhoat (1997), An advective-reflective conceptual model for the oscillatory nature of the ENSO, *Science*, *277*, 663–666.

Picaut, J., E. Hackert, A. J. Busalacchi, R. Murtugudde, and G. S. E. Lagerloef (2002), Mechanisms of the 1997–1998 El Niño–La Niña, as inferred from space-based observations, *J. Geophys. Res.*, *107*(C5), 3037, doi:10.1029/2001JC000850.

Pond, S., and G. Pickard (1983), *Introductory Dynamical Oceanography*, 329 pp., Elsevier, New York.

Rasmusson, E. M., and T. H. Carpenter (1982), Variations in tropical sea surface temperature and surface wind fields associated with the Southern Oscillation/El Niño, *Mon. Weather Rev.*, *110*(5), 354–384.

Rébert, J. P., J. R. Donguy, G. Eldin, and K. Wyrtki (1985), Relations between sea level, thermocline depth, heat content, and dynamic height in the tropical Pacific Ocean, *J. Geophys. Res.*, *90*(C6), 11,719–11,725.

Reynolds, R., N. Rayner, T. Smith, D. Stokes, and W. Wang (2002), An improved in situ and satellite SST analysis for climate, *J. Clim.*, *15*, 1609–1625.

Ridgway, K. R., J. S. Godfrey, G. Meyers, and R. Bailey (1993), Sea level response to the 1986–1987 El Niño-Southern Oscillation event in the western Pacific in the vicinity of Papua New Guinea, *J. Geophys. Res.*, *98*(C9), 16,387–16,395.

Slingo, J. M., D. P. Rowell, K. R. Sperber, and F. Nortley (1999), On the predictability of the interannual behavior of the Madden-Julian oscillation and its relationship with El Niño, *Q. J. R. Meteorol. Soc.*, *125*, 583–609.

Springer, S., M. McPhaden, and A. Busalacchi (1990), Oceanic heat content in the tropical Pacific during the 1982–1983 El Niño, *J. Geophys. Res.*, *95*(C12), 22,089–22,101.

Suarez, M. J., and P. S. Schopf (1988), A delayed action oscillator for ENSO, *J. Atmos. Sci.*, *45*, 3283–3287.

Terray, P., and S. Dominiak (2005), Indian ocean sea surface temperature and El Niño–Southern Oscillation: A new perspective, *J. Clim.*, *18*, 1351–1368, doi:10.1175/JCLI3338.1.

Trenberth, K. E., and D. P. Stepaniak (2001), Indices of El Niño evolution, *J. Clim.*, *14*(8), 1697–1701.

Wakata, Y., and E. Sarachik (1991), On the role of equatorial ocean modes in the ENSO cycle, *J. Phys. Oceanogr.*, *21*, 434–443.

Wang, B. (1995), Interdecadal changes in El Niño onset in the last four decades, *J. Clim.*, *8*(2), 267–285.

Wang, C. (2001), A unified oscillator model for the El Niño–Southern Oscillation, *J. Clim.*, *14*, 98–115.

Wang, C., and J. Picaut (2004), Understanding ENSO physics—A review, in *Earth's Climate: The Ocean-Atmosphere Interaction*, pp. 21–48, AGU, Washington, D. C.

Weisberg, R. H., and C. Z. Wang (1997), A western Pacific oscillator paradigm for the El Niño Southern Oscillation, *Geophys. Res. Lett.*, *24*(7), 779–782.

Wyrtki, K. (1985), Water displacements in the Pacific and the genesis of El Niño cycles, *J. Geophys. Res.*, *90*(C4), 7129–7132.

Xu, J., and J. C. L. Chan (2001), The role of the Asian–Australian monsoon system in the onset time of El Niño events, *J. Clim.*, *14*(3), 418–433.

Zebiak, S. (1989), Ocean heat content variability and ENSO cycles, *J. Phys. Oceanogr.*, *19*, 475–485.

Zebiak, S. E., and M. A. Cane (1987), A model of El Niño-Southern Oscillation, *Mon. Weather Rev.*, *115*, 2262–2278.

————————————

C. Bosc and T. Delcroix, Laboratoire d'Etudes en Géophysique et Océanographie Spatiales (LEGOS), UMR 5566, CNES/CNRS/IRD/UPS, 14, Avenue Ed. Belin, 31400 Toulouse, France. (thierry.delcroix@ird.fr)